THE MEGASECOND *CHANDRA* X-RAY VISIONARY PROJECT OBSERVATION OF NGC 3115. III. LUMINOSITY FUNCTIONS OF LMXBS AND DEPENDENCE ON STELLAR ENVIRONMENTS

DACHENG LIN[1,2], JIMMY A. IRWIN[1], KA-WAH WONG[3], ZACHARY G. JENNINGS[4], JEROEN HOMAN[5], AARON J. ROMANOWSKY[4,6], JAY STRADER[7], JEAN P. BRODIE[4], GREGORY R. SIVAKOFF[8], AND RONALD A. REMILLARD[5]

[1] Department of Physics and Astronomy, University of Alabama, Box 870324, Tuscaloosa, AL 35487, USA
[2] Space Science Center, University of New Hampshire, Durham, NH 03824, USA; dacheng.lin@unh.edu
[3] Eureka Scientific, Inc., 2452 Delmer Street Suite 100, Oakland, CA 94602-3017, USA
[4] University of California Observatories, Santa Cruz, CA 95064, USA
[5] MIT Kavli Institute for Astrophysics and Space Research, MIT, 70 Vassar Street, Cambridge, MA 02139-4307, USA
[6] Department of Physics and Astronomy, San José State University, One Washington Square, San José, CA 95192, USA
[7] Department of Physics and Astronomy, Michigan State University, East Lansing, Michigan, MI 48824, USA
[8] Department of Physics, University of Alberta, Edmonton, Alberta, T6G 2E1, Canada

ABSTRACT

We studied the X-ray luminosity function (XLF) of low-mass X-ray binaries (LMXBs) in the nearby lenticular galaxy NGC 3115, using the Megasecond *Chandra* X-ray Visionary Project Observation. With a total exposure time of $\sim$1.1 Ms, we constructed the XLF down to a limiting luminosity of $\sim 10^{36}$ erg s^{-1}, which is much deeper than that typically reached for other early-type galaxies. We found significant flattening of the overall LMXB XLF from $dN/dL \propto L^{-2.2\pm0.4}$ above 5.5×10^{37} erg s^{-1} to $dN/dL \propto L^{-1.0\pm0.1}$ below it, although we could not rule out a fit with a higher break at $\sim 1.6 \times 10^{38}$ erg s^{-1}. We also found evidence that the XLF of LMXBs in globular clusters (GCs) is overall flatter than that of field LMXBs. Thus, our results for this galaxy do not support the idea that all LMXBs are formed in GCs. The XLF of field LMXBs seems to show spatial variation, with the XLF in the inner region of the galaxy being flatter than that in the outer region, probably due to contamination of LMXBs from undetected and/or disrupted GCs in the inner region. The XLF in the outer region is probably the XLF of primordial field LMXBs, exhibiting $dN/dL \propto L^{-1.2\pm0.1}$ up to a break close to the Eddington limit of neutron star LMXBs ($\sim 1.7 \times 10^{38}$ erg s^{-1}). The break of the GC LMXB XLF is lower, at $\sim 1.1 \times 10^{37}$ erg s^{-1}. We also confirm previous findings that the metal-rich/red GCs are more likely to host LMXBs than the metal-poor/blue GCs, which is more significant for more luminous LMXBs, and that more massive GCs are more likely to host LMXBs.

Key words: Galaxy: stellar content – globular clusters: general – X-rays: binaries – X-rays: individual (NGC 3115)

1. INTRODUCTION

Population studies of X-ray binaries in nearby galaxies are possible thanks to the superb spatial resolution and excellent sensitivity of the *Chandra X-ray Observatory* (Weisskopf et al. 2002). The X-ray luminosity functions (XLFs) of point sources have been obtained for many galaxies, and they are found to be environment dependent (see Fabbiano 2006, for a review). In young normal galaxies, high-mass X-ray binaries (HMXBs) dominate, and the XLFs follow a simple power law (PL) $dN/dL_X \propto L_X^{-\alpha}$ with $\alpha \approx 1.6$ over a large range of luminosity: 10^{35} erg s$^{-1} \lesssim L_X \lesssim 10^{40}$ erg s^{-1} (Grimm et al. 2003; Mineo et al. 2012). In old normal galaxies or in the bulge of young normal galaxies, low-mass X-ray binaries (LMXBs) dominate and the XLFs seem relatively complicated, showing both a high-luminosity break at $L_X \sim 5 \times 10^{38}$ erg s^{-1} (Sarazin et al. 2001; Gilfanov 2004; Kim & Fabbiano 2004; Zhang et al. 2012) and a low-luminosity break at $L_X \sim 5 \times 10^{37}$ erg s^{-1} (Gilfanov 2004; Kim et al. 2009; Voss et al. 2009; Luo et al. 2012; Zhang et al. 2012). The slope between these two breaks is $\alpha \approx 1.8$–2.2. Above the high-luminosity break the XLFs decrease sharply. Below the low-luminosity break the XLFs might flatten to $\alpha \approx 1.0$.

The high-luminosity break may be due to the Eddington limit of neutron star (NS) LMXBs. The low-luminosity break has been attributed to either the transition from mass transfer driven by magnetized stellar wind at high luminosities to mass transfer driven by gravitational wave emission at low luminosities (Postnov & Kuranov 2005), or different types of

donor stars, with the high-luminosity ones being giants and the low-luminosity ones being main-sequence stars (Revnivtsev et al. 2011). The former predicts the slope below the break to be about 1.0 and the slope above the break to be about 2.0. For the latter explanation, the steepening of the XLF at high luminosity is due to the short lifetime of binary systems with giants.

The XLFs of LMXBs have often been obtained by combining multiple galaxies in order to improve the statistics. However, this method is subject to the limitation that the normalizations of the XLFs in different galaxies show a scatter of more than a factor of two (Zhang et al. 2012). The XLFs of LMXBs well below 10^{37} erg s^{-1} are still only obtained for very few old galaxies, most notably Centaurus A and NGC 3379 (Kim et al. 2009; Voss et al. 2009), and the bulge of M31 (Voss & Gilfanov 2007a, 2007b). A low detection limit is critical for constraining the low-luminosity break, which has been shown mostly for the old populations in young galaxies (Fabbiano 2006). Deep observations of old galaxies are also needed for the investigation of the differences between the XLFs of LMXBs in globular clusters (GCs) and the stellar field, which can be used to check whether they have the same origin. For instance, there is a relative underabundance of faint LMXBs in GCs when compared with field LMXBs (Kim et al. 2009; Voss et al. 2009; Zhang et al. 2011).

NGC 3115 was selected as the target of a 1 Ms *Chandra* X-ray Visionary Project (XVP) in Cycle 13. One main goal was to study the gas flow inside the Bondi radius of the central

Table 1
Observation Log

Notation	Obs. ID	Date	Exposure (ks)	Offset[a] (arcmin)
1	2040	2001 Jun 14	35.8	1.5
2	11268	2010 Jan 27	40.6	0.1
3	12095	2010 Jan 29	75.6	0.1
4	13817	2012 Jan 18	171.9	0.0
5	13822	2012 Jan 21	156.6	0.0
6	13819	2012 Jan 26	72.9	0.0
7	13820	2012 Jan 31	184.1	0.0
8	13821	2012 Feb 03	157.9	0.0
9	14383	2012 Apr 04	119.4	0.3
10	14419	2012 Apr 05	46.3	0.3
11	14384	2012 Apr 06	69.7	0.3

Note.
[a] Aim point offset from observation 13820.

supermassive black hole (BH), which was reported in Wong et al. (2014). The other goal was to take a deep look at the X-ray binary population of a normal early-type galaxy. The detailed analysis of the data, including the source list and detailed properties of special sources, will be presented in Lin et al. (2015, Paper II hereafter). In the present paper, we concentrate on the XLF of LMXBs, especially on its faint end below 10^{37} erg s^{-1}. NGC 3115 is a lenticular (S0) galaxy with an age of 8.4 ± 1.1 Gyr (Sánchez-Blázquez et al. 2006), at a distance of 9.7 Mpc (Tonry et al. 2001). Including previous observations, the total exposure time of *Chandra* on this galaxy is ~1.1 Ms, reaching a limiting luminosity of ~10^{36} erg s^{-1}. Thus it is one of the best observed normal early-type galaxies by *Chandra*. Accompanying the *Chandra* XVP observation is a six pointing *Hubble Space Telescope* (*HST*) mosaic observation in the F475W and F850LP filters (hereafter *g* and *z* filters, respectively) using the Advanced Camera for Surveys (ACS). It provides information about GCs in the galaxy (Jennings et al. 2014), which we use to investigate the dependence of the XLF of LMXBs on the stellar environment.

The paper is organized as follows. In Section 2, we describe the X-ray data reduction, construction of XLFs, incompleteness correction, and cross-correlation of the X-ray and optical sources. In Section 3, we show the spatial distributions of different populations, present the total LMXB XLF, compare the XLFs of GC and field LMXBs, and investigate the GC LMXB properties. In Section 4, we discuss various caveats on the XLFs that we obtain and the implication of our results for the nature and formation of LMXBs. Our conclusions are given in Section 5.

2. DATA ANALYSIS

2.1. Observations and Source Detection

The *Chandra* observations of NGC 3115 are listed in Table 1. There are 11 observations in total from essentially three epochs: one in 2001, two in 2010, and nine in 2012. All observations used the imaging array of the AXAF CCD Imaging Spectrometer (ACIS; Bautz et al. 1998). The reduction of the data and the creation of the source list were presented in detail in Paper II, and here we briefly summarize the procedure adopted. The data were analyzed with the *Chandra* Interactive Analysis of Observations (CIAO, version

4.6) package. The data were reprocessed to apply the latest calibration (CALDB 4.5.9) and the subpixel algorithm (Li et al. 2004) using the CIAO script *chandra_repro*. Some short background flares seen in observations 2040, 13819, and 13822 were excluded. The final exposure used for each observation is given in Table 1. The relative astrometry between the observations was corrected, and a source detection was performed on individual observations as well as on the merged one using the 0.5–7 keV energy band with the CIAO *wavdetect* wavelet-based source detection algorithm (Freeman et al. 2002). We used two different image binning resolutions: one at single sky pixel resolution (0″.492) over the full field of view (FOV) and the other at 1/8 sky pixel resolution covering an area of $3' \times 3'$ centered at the center of NGC 3115. The subpixel binning images were used to improve the spatial resolution of the crowded field near the center of the galaxy. Sources detected from the merged observation and individual observations were cross-correlated to create the final unique source list.

For each unique source, we extracted the source and background spectra, and created the response file for each individual observation. These were then merged to create the spectra and response files for the merged observation. The source region was set to be a circle enclosing 90% of the point-spread function (PSF) at 2.3 keV. The background region was set to be a concentric annulus, with inner and outer radii of two and five times the source radius, respectively. The background-subtracted 0.5–7 keV count rates were then converted to unabsorbed fluxes and luminosities, with the conversion factors based on the corresponding response files and assuming an absorbed PL spectral shape with a photon index of 1.7 and the Galactic absorption $N_{\mathrm{H}} = 4.32 \times 10^{20}$ cm^{-2} (Kalberla et al. 2005).

2.2. Incompleteness Calculation and XLF Construction

The point-source detection sensitivity varies across the *Chandra* image, owing to the position dependence of the diffuse X-ray emission in the galaxy, the PSF extent, the exposure, and CCD efficiency. Therefore it is necessary to carry out the incompleteness correction for the XLF. The D_{25} region of NGC 3115 has a semimajor axis of $a = 3'.62$ (10.2 kpc), a semiminor axis of $b = 1'.23$ (3.5 kpc), and a position angle of 40° (de Vaucouleurs et al. 1991). To limit the incompleteness effects and the cosmic X-ray background (CXB) contribution, we defined our study field for the XLF of a field LMXBs as the region inside D_{25}. Further considering that the central region is very crowded and has strong diffuse X-ray emission, we excluded the central $a = 10''$ elliptical region (the eccentricity and position angle follow the D_{25} ellipse) for all XLFs throughout the paper.

We calculated the incompleteness function $K(L)$—the fraction of pixels weighted by the assumed spatial distribution of sources in which a source with the luminosity L or higher would be detected—using the backward correction method (Kim & Fabbiano 2003). In this method, sources are simulated with MARX and added one by one to the real observed image, which is then checked to see whether each one could be detected with *wavdetect*. The source spectral shape was assumed to be a PL with a photon index of 1.7 and the Galactic absorption. The simulations were carried out for a series of luminosities with an increasing factor of 1.1 and 1.21 below and above the 90% completeness luminosity, respectively. The
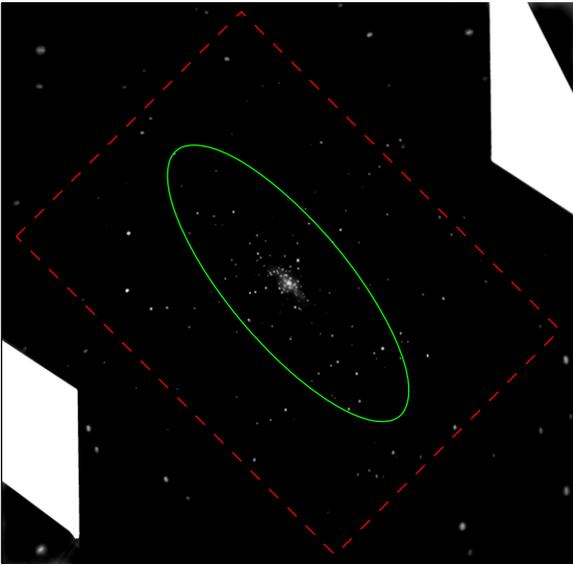
Figure 1. *Chandra* X-ray image of NGC 3115 in 0.5–7 keV. The image is adaptively smoothed with the CIAO task csmooth and exposure corrected. The D_{25} ellipse of the galaxy and the approximate FOV of the *HST*/ACS mosaic observation (dashed box) are also shown.

positions of simulated sources for each luminosity were specified as follows: The D_{25} ellipse was divided into elliptical annuli with a series of ellipses that have the eccentricity and position angle following D_{25} and semimajor axis a for the ith ($i = 0$–56) ellipse assuming $a_i = a_{i-1} + \delta a * 1.04^{i-1}$, where $a_0 = 10''$ and $\delta a = 1''$. Each elliptical annulus was then divided into 80 cells with an equal area, and the simulated source position was specified at the center of each cell, with 4,560 in total. In some cases, the simulated sources coincided with the real sources; we assumed that the simulated sources were detected by *wavdetect* only if the simulated sources dominated the flux over the real sources, which was to take the source confusion effect into account. We calculated $K(L)$ for the CXB sources and field LMXBs separately, because the CXB sources have a flat distribution and the field LMXBs are expected to follow the K_S-band light (Gilfanov 2004), for which we used the 2MASS Large Galaxy Atlas data (Jarrett et al. 2003).

We also calculated $K(L)$ for GC LMXBs. We used all the GCs detected in the optical (Section 2.3) as the parent spatial distribution of GC LMXBs, and assumed that they have equal probability of hosting an LMXB. To limit the incompleteness effects and spurious rate of the GC LMXB identification, our study field for the XLF of GC LMXBs was set to the *HST*/ACS FOV. The *HST*/ACS FOV reached $\sim 1.3 D_{25}$ and $\sim 2.5 D_{25}$ in the major-axis and minor-axis directions of the D_{25} ellipse, respectively (Figure 1).

The differential XLF of LMXBs in a given region can be calculated as follows (refer to, e.g., Voss et al. 2009):

$$\frac{dN_{\mathrm{LMXB}}}{dL} = \frac{1}{K_{\mathrm{LMXB}}(L)}$$
$$\times \left(\frac{dN_{\mathrm{obs}}}{dL} - 4\pi D^2 K_{\mathrm{CXB}}(L) \frac{dN_{\mathrm{CXB}}}{dL} \right), \qquad (1)$$

where N_{obs} is the total number of observed sources and D is the distance to NGC 3115. The quantity $4\pi D^2 \, dN_{\mathrm{CXB}}/dL$ is dN_{CXB}/dS, which is the $\log(N)$–$\log(S)$ distribution of the

CXB sources. We used the full band (0.5–10 keV) $\log(N)$–$\log(S)$ distribution of CXB sources from Georgakakis et al. (2008), with their 0.5–10 keV flux converted to our 0.5–7 keV band, assuming a PL spectrum with a photon index of 1.4. For the XLF of field LMXBs only, we filtered out GC LMXBs and had the CXB contribution estimated as described previously. For the XLF of GC LMXBs, the CXB contribution was not corrected because it is negligibly small.

We did not correct XLFs for the HMXB contribution. Following Mineo et al. (2012), we estimated the star-formation rate in NGC 3115 to be $0.07 \, M_\odot \, \mathrm{yr}^{-1}$ (see their Equation (9), which is based on the UV and IR emission). Based on their XLF for HMXBs (their Equation (18)), we can estimate the number of HMXBs in NGC 3115 above L_{lim} to be 2.3, which is one order of magnitude less than the CXB contribution and is thus negligibly small.

To compare with previous studies, some XLFs presented in this study will be divided by (and thus normalized to) the stellar mass enclosed in our study region of the field LMXB XLF (i.e., within D_{25} and outside the central $a = 10''$ ellipse). Following Zhang et al. (2012), we used the K_s-band luminosity and estimated the stellar mass in our study region to be $6.31 \times 10^{10} \, M_\odot$ (the total stellar mass within D_{25} is $7.83 \times 10^{10} \, M_\odot$).

2.3. Multiwavelength Cross-correlation

We cross-correlated our X-ray sources with optical sources from *HST*/ACS mosaic imaging and Subaru/Suprime-Cam imaging to search for the GC LMXBs. Jennings et al. (2014) compiled 360 GC candidates from *HST*/ACS mosaic imaging and an additional 421 from Subaru/Suprime-Cam imaging (Arnold et al. 2011). Before cross-correlation, we first carried out absolute astrometry correction on X-ray sources by cross-correlating their positions with the 360 GC candidates from the *HST*/ACS mosaic imaging, whose astrometry was registered to the USNO-B1.0 Catalog (Monet et al. 2003). We only used X-ray sources detected at $>6\sigma$ significance and with off-axis angles $<6'$ (the limit of *HST*/ACS FOV) in the cross-correlation. We found 30 matches with a median separation residual of $0''.06$.

We searched for the *HST*/ACS GC counterparts to our X-ray sources using the 99.73% (i.e., 3σ) positional uncertainty that combines both X-ray and optical components. For the *HST*/ACS sources, we assumed the half-light radius as the 1σ positional uncertainty. We also included a systematic uncertainty which was assumed to be $0''.05$ (1σ, in both R.A. and decl.) based on the above matches in the absolute astrometry correction. This systematic uncertainty is probably over-estimated, but it is so small that the number of GC matches remained the same even if we did not include this systematic uncertainty. The offsets of all matches (37 in total) are $<1''$ (only 3 have offsets $>0''.2$) and have a median of $0''.07$. To estimate the spurious rate, we rotated the *HST*/ACS field by $\pm 10°$, $180° \pm 10°$, and $180°$ around the galaxy center and carried out the cross-correlation in the same way; we found the spurious rate to be about 3%.

The *HST*/ACS GC distribution from Jennings et al. (2014) decreases sharply within $\sim 0.25 D_{25}$ (see Section 3.1). Therefore their GC list is probably fairly incomplete in this region owing to strong stellar light. We tried to match our X-ray sources with the sources that were detected by Jennings et al. (2014) but not

classified as GCs, and we found three extra matches (S12, S53, and S79 in Paper II) within $0.25D_{25}$. One more source (S65) seems to have an optical match from our visual inspection, but it is not detected by Jennings et al. (2014) due to its being too close to the galaxy center ($5''.5$, within the $a = 10''$ elliptical exclusion region). We classify these four sources as GC LMXB candidates. They are all bright ($>10^{37}$ erg s^{-1}) and are not expected to be CXB sources (the expected CXB source number at this luminosity is 0.5 and is much smaller if only CXB sources with bright optical counterparts are considered). Another source (S92 in Paper II) outside $0.25D_{25}$ also has an optical match, but it was classified as a star by Jennings et al. (2014) due to the measurement of a radial velocity (238 km s^{-1}), which was much lower than the threshold of 350 km s^{-1} that they adopted to define GCs. Considering that the size and color of this optical match are both consistent with typical GCs, we treat it as a GC LMXB candidate too. However, we did not include these five LMXBs in either field or GC XLFs (although S65 is outside the study region and would not be included anyway).

In our search for the GC optical counterparts to our sources detected only in the Subaru/Suprime-Cam imaging (i.e., not in the *HST*/ACS imaging), we also used the 99.73% positional uncertainty. The 1σ positional uncertainty of the optical sources was assumed to be $0''.1$ in both R.A. and decl. The 1σ systematic uncertainty was assumed to be $0''.1$ in both R.A. and decl. (Paper II). To limit the spurious rate, we have a maximum searching radius of $2''$. The spurious rate was estimated to be 5% (Paper II). Only eight Subaru/Suprime-Cam GC matches were found; they are used only for the study of the spatial distribution of GC LMXBs in Section 3.1, but not for the study of XLFs.

3. RESULTS

3.1. Spatial Distribution

Figure 1 shows the *Chandra* X-ray image of NGC 3115. From the merged observation, we detected 145 X-ray sources above the 50% completeness luminosity $L_{\rm lim} = 1.21 \times 10^{36}$ erg s^{-1} (Section 3.2) within D_{25} and outside the central $a = 10''$ ellipse (23 within this exclusion region). The expected CXB source number is 26.5.

Figure 2 shows the cumulative radial distributions of different classes of objects detected from the merged observation. Due to the high inclination ($i = 86°$, Capaccioli et al. 1987) of NGC 3115, we plot the distributions with respect to α/R_{25}, where α is the angular separation between the source and the galaxy center, and R_{25} is the elliptical radius of the D_{25} isophotal ellipse in the direction from the galaxy center to the source. The cumulation starts at $\alpha/R_{25} = 0.046$ because we excluded the central $a = 10''$ elliptical region in the calculation of XLFs. To reduce the incompleteness effects, we used only sources above 4×10^{36} erg s^{-1}, which is the 82% completeness luminosity for CXB sources and the 94% completeness luminosity for field LMXBs within $2D_{25}$ (but outside the central $a = 10''$ elliptical region). The non-GC X-ray sources, which are expected to consist of field LMXBs and CXB sources mostly (red solid line), and GC LMXBs (red dotted–dashed line), are plotted separately. The thick blue dotted line models the spatial distribution of non-GC X-ray sources using two components, one for CXB sources and the other for field LMXBs, which were assumed to follow the IR
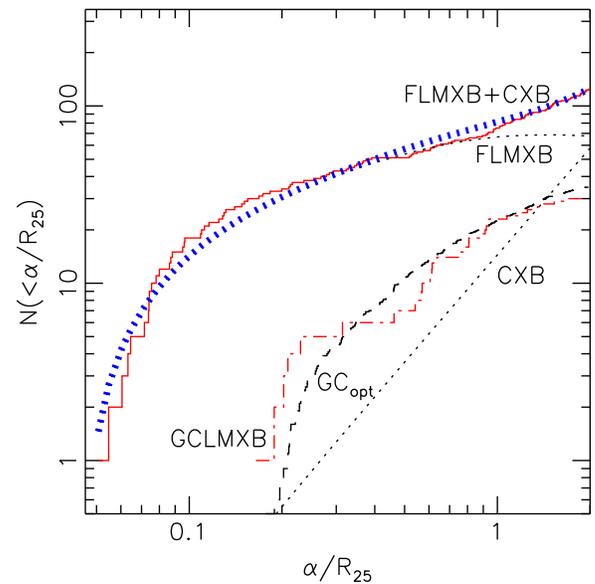

Figure 2. Radial distribution of observed sources excluding GC LMXBs (red solid line), compared to the model (thick blue dotted line) composed of field LMXBs (FLMXB) and CXB sources (thin dotted line). Also plotted are the radial distributions of GC LMXBs (red dotted–dashed line) and the optical GCs (dashed line, divided by a factor of 10). The cumulation starts at $\alpha/R_{25} = 0.046$ (i.e., excluding the central $a = 10''$ elliptical region) and ends at $2D_{25}$. To reduce the incompleteness effects, only sources with $L_X \geqslant 4.0 \times 10^{36}$ erg s^{-1} are used.

light in the K_s band. The normalization of the field LMXB component was determined so as to give the same number of sources, after adding the CXB component, as observed within $2D_{25}$. The observed distribution roughly follows this model, with the Kolmogorov–Smirnov (K–S) test giving a probability of 30%. The radial distribution of GC LMXBs seems to approximately follow that of GCs detected in the optical as well, with the K–S test giving a probability of 62%.

Figure 2 shows a dramatic difference between the spatial distributions of field and GC LMXBs. The field LMXBs tend to cluster toward the galaxy center, while GC LMXBs tend to be more spread out. Only seven out of 360 *HST*/ACS GCs are within $0.2D_{25}$. However, we note that the GC detection is probably fairly incomplete near the galaxy center due to strong stellar light. Some GCs could also be destroyed near the galaxy center due to mass segregation.

There are 50 non-GC X-ray sources above 4×10^{36} erg s^{-1} that are observed between D_{25} and $2D_{25}$, while the expected number of CXB sources is 40.2 after incompleteness correction and the expected number of field LMXBs is 1.5 based on the IR light in the K_s band. The 50 non-GC X-ray sources include two special sources: S109 and S179 (Paper II). The former is a supersoft X-ray source (SSS) at $1.53D_{25}$. The latter is a transient with 0.5–7 keV long-term variability factor $V_{\rm var} > 20$ and relatively soft X-ray spectra (classified as a BH X-ray binary candidate in Paper II), and it is at $1.04D_{25}$. Therefore, these two sources are most probably in NGC 3115 instead of being CXB sources. The remaining total of 48 is still 19% more than the expected number of CXB sources. If we concentrate on the region between $1.3D_{25}$ and $2D_{25}$ (there is little IR light outside $1.3D_{25}$ from the galaxy), we have 33 non-GC X-ray sources above 4×10^{36} erg s^{-1}, excluding S109, which is very close to the expected number of CXB sources (30.6, incompleteness corrected).
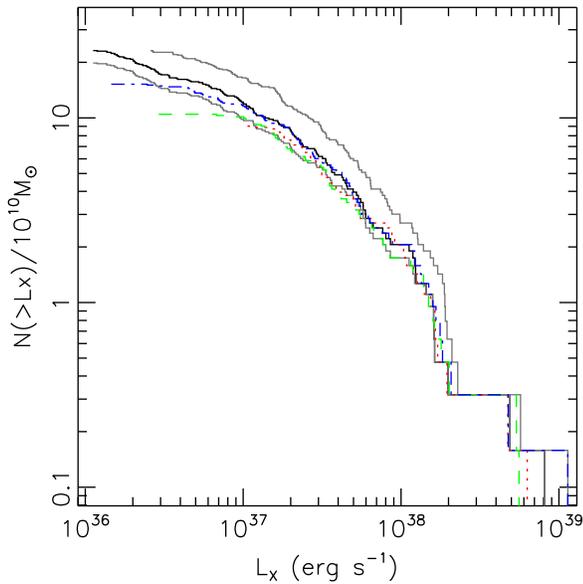
Figure 3. Cumulative XLFs from the merged observation (black solid line) and single observations 2040 (red dotted line), 12095 (green dashed line), and 13820 (blue dotted–dashed line). The gray solid line is also from the merged observation but using sources with $V_{\mathrm{var}} < 5.0$. The gray dotted–dotted–dashed line uses the maximum luminosity of each source. The distributions are not corrected for incompleteness or the CXB contribution.

3.2. The XLF of All LMXBs

Because a large fraction of our sources is variable, we first check whether there is any difference in the XLFs between observations. We plot the observed cumulative XLFs for the merged observation and the longest observation in each of the three epochs in Figure 3. We compared their XLFs using the K–S test. We focused on luminosities above the 90% completeness limit, which are 3.3×10^{37}, 1.6×10^{37}, and 8.6×10^{36} erg s^{-1} for observations 2040, 12095, and 13820, respectively. We found that the XLFs obtained in these individual observations are consistent with the same distributions obtained in the merged observation with the K–S probability of 48%, 98%, and 82%, respectively. Voss et al. (2009) obtained a similar conclusion for Centaurus A. We also constructed the XLF using less variable sources (the 0.5–7 keV flux long-term variability $V_{\mathrm{var}} < 5$, Paper 1) in the merged observation (gray solid line in Figure 3) and compared it with the XLF using all sources. Above the luminosity at the 90% completeness level (2.7×10^{36} erg s^{-1}), the K–S test also indicates no obvious difference between them, with the probability of 100%. Finally, we constructed the XLF using the maximum luminosity of each source (gray dotted–dotted–dashed line in Figure 3). When we compared it with the XLF from the merged observation and limited to $L > 2.7 \times 10^{36}$ erg s^{-1}, the K–S test gave a probability of 37%. From all these comparisons, we see no significant effect of the source long-term variability on the XLFs. Therefore, hereafter we use the mean luminosities of the sources detected from the merged observations for the XLFs.

The incompleteness functions for (field) LMXBs and CXB sources are shown in Figure 4. While they appear to be similar to one another, this is a coincidence, because they can be very different if different regions other than the whole D_{25} (excluding the central $a = 10''$ ellipse) are used. The luminosity corresponding to the 50% completeness level is about
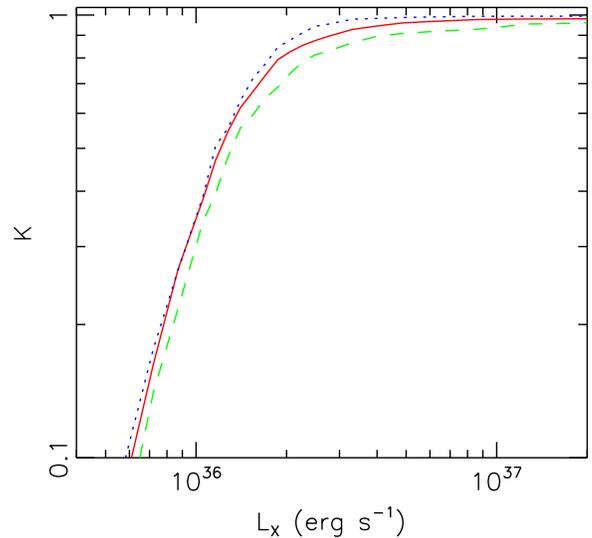

Figure 4. Incompleteness functions for field LMXBs (red solid line), GC LMXBs (green dashed line), and CXB sources (blue dotted line).

$L_{\mathrm{lim}} = 1.21 \times 10^{36}$ erg s^{-1}, which is much lower than the typical values of $\sim 10^{37}$ erg s^{-1} achieved for other galaxies by *Chandra* (e.g., Zhang et al. 2012). Above this luminosity limit, the sources detected in the merged observation within D_{25} are all $>2.9\sigma$.

The incompleteness corrected and CXB contribution subtracted XLF above L_{lim} for all LMXBs is plotted in the left panels in Figure 5. The XLF is steep down to a break around 5×10^{37} erg s^{-1}, below which the XLF flattens clearly. We fitted the differential form of XLF with a small L_{X} bin size of $\delta \log(L_{\mathrm{X}}) = 0.02$ using the C statistic (which is maximum likelihood-based) in the Xspec fitting package (Arnaud 1996). In this way, the observed XLF was used in the fit, but the fitting model was modified by the incompleteness function (through a response file). The model that we adopted is a broken PL:

$$\frac{dN}{dL_{36}} = \begin{cases} K\, L_{36}^{-\alpha_1}, & L_{36} < L_{\mathrm{b}} \\ K\, L_{\mathrm{b}}^{\alpha_2-\alpha_1} L_{36}^{-\alpha_2}, & L_{36} > L_{\mathrm{b}} \end{cases}, \qquad (2)$$

where $L_{36} = L_{\mathrm{X}}/(10^{36}$ erg s$^{-1})$. We obtained $\alpha_1 = 1.03^{+0.10}_{-0.14}$, $\alpha_2 = 2.2^{+0.3}_{-0.4}$, and $L_{\mathrm{b}} = 55^{+12}_{-23}$ (Table 2 and Figure 5 (green solid line)).

Zhang et al. (2012) fitted the average XLF of 20 early-type galaxies with the template introduced by Gilfanov (2004), which is essentially a double broken PL. Because we do not have enough statistics above the second break that they obtained (6×10^{38} erg s^{-1}), we do not need to introduce the second break to fit our XLF. Our fit is fully consistent with that obtained by Zhang et al. (2012), who reported $\alpha_1 = 1.02 \pm 0.08$, $\alpha_2 = 2.06 \pm 0.06$, and $L_{\mathrm{b}} = 54.6 \pm 4.0$. The main difference is the normalization K, with ours being about 76% of that of Zhang et al. (2012), after being normalized by stellar mass (our $K = 4.6 \pm 1.3$ per $10^{10} M_{\odot}$ versus their $K = 6.0 \pm 1.7$ per $10^{10} M_{\odot}$). This is consistent with the result obtained by Zhang et al. (2012) that NGC 3115 has a relatively low number of LMXBs per unit stellar mass compared with other galaxies they had studied (NGC 3115 was included in their galaxy sample with only the first three observations analyzed). Their fit with the normalization decreased by 24% is also shown in Figure 5 (blue dashed line).
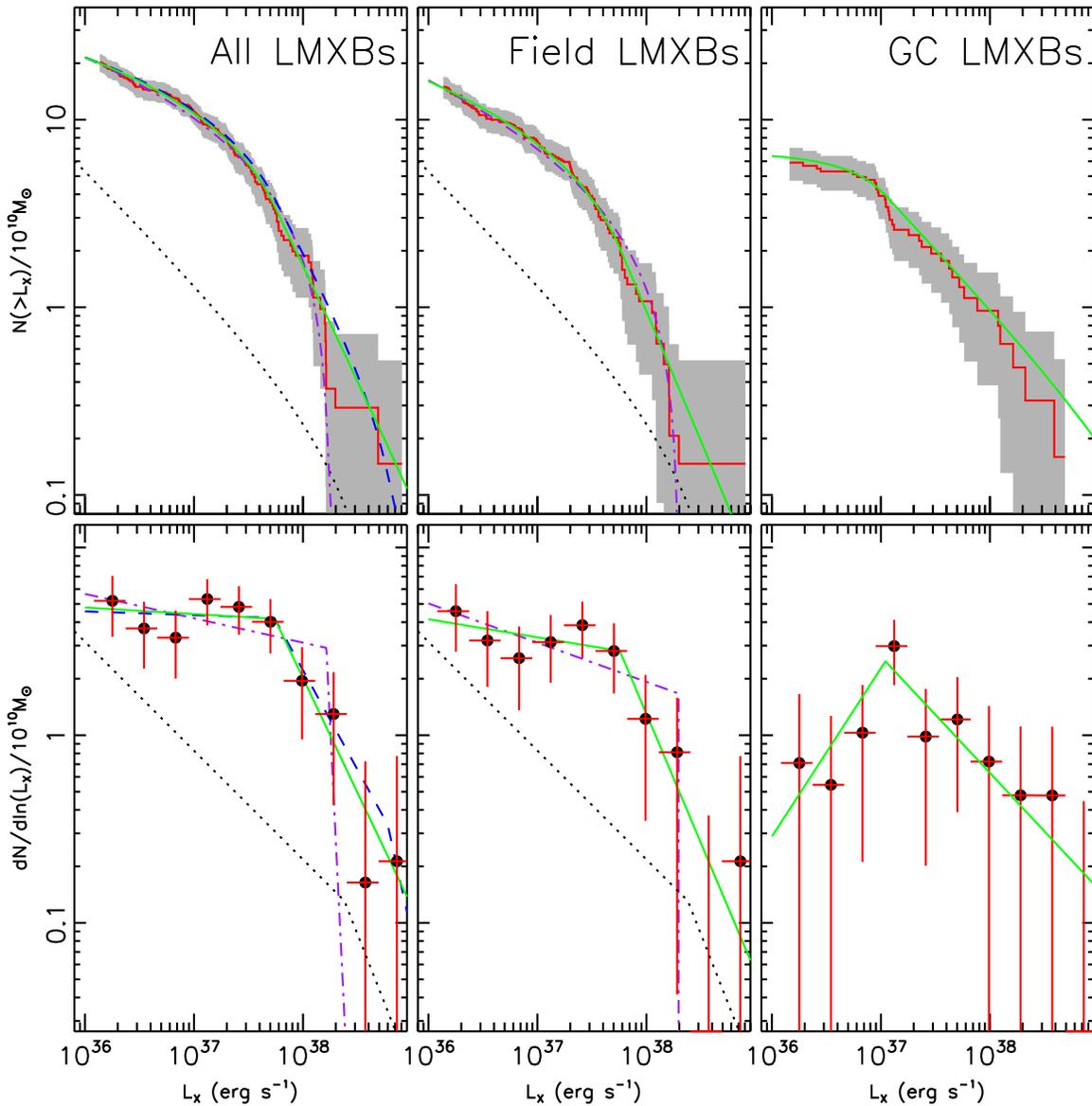
Figure 5. Incompleteness corrected and CXB contribution subtracted XLFs for all LMXBs (left panels), field LMXBs (middle panels), and GC LMXBs (right panels). We plot both the cumulative (upper panels; the red solid line with the shaded area representing 1σ Poissonian uncertainty) and differential forms (lower panels). Our fits with a broken PL are shown as green solid lines (the low-break solution) and purple dotted–dashed lines (the high-break solution, when present, see the text). We note that the high-break solutions have a large uncertainty in the second index, whose lower limit is given in Table 2. The dashed blue lines in the left panels are the fit to the average XLF of 20 early-type galaxies by Zhang et al. (2012), with the normalization decreased by 24%. The black dotted line is the expected CXB distribution.

We note that we found a high-break fit (Table 2, purple dotted–dashed line in Figure 5) that gives a higher break luminosity ($(1.6 \pm 0.1) \times 10^{38}$ erg s^{-1}), a much steeper second slope (>6.4, 1σ lower limit), and has a C statistic only larger than the above low-break fit by 1.1. The initial slope of the high-break fit (1.13 ± 0.08) is slightly higher than that of the low-break fit.

3.3. The XLF of LMXBs in the Field

The incompleteness corrected and CXB contribution subtracted XLF above L_{lim} for LMXBs in the field is plotted in the middle panels in Figure 5. The results of our fit with a broken PL are given in Table 2. As for the XLF of all LMXBs, we also find a low-break fit and a high-break fit to the XLF of field LMXBs. The low-break fit has a C statistic higher than the

high-break fit by only 0.3. The parameters of both fits are very similar to the corresponding fits to the XLF of all LMXBs (Section 3.2), probably due to relatively few GC LMXBs in the total sample. Figure 5 shows both the low-break fit (green solid line) and the high-break fit (purple dotted–dashed line) to the field LMXB XLF.

To check whether there is spatial variation of the XLF of field LMXBs, we divided our study field into an inner ($(0.046–0.2) D_{25}$) and outer ($(0.2–1.0) D_{25}$) region (the boundary was chosen to ensure enough statistics in both regions) and created two corresponding XLFs. These are shown in Figure 6. It is nontrivial to use the K–S test to compare these two XLFs due to their different CXB and incompleteness corrections. Therefore, we also fitted them with a broken PL for comparison. The fitting results are shown in

Table 2
The Maximum Likelihood Fits to XLFs of Different Populations
Using a Broken Power Law

Population (1)	$N_{\rm tot}$ (2)	$N_{\rm CXB}$ (3)	α_1 (4)	α_2 (5)	$L_{\rm b}$ (6)	K (7)
Total	145	26.5	$1.03^{+0.10}_{-0.14}$	$2.2^{+0.3}_{-0.4}$	55^{+12}_{-23}	30^{+9}_{-9}
			$1.13^{+0.08}_{-0.08}$	>6.7	164^{+13}_{-8}	36^{+9}_{-7}
Field	114	26.5	$1.10^{+0.12}_{-0.13}$	$2.4^{+0.5}_{-0.5}$	57^{+17}_{-24}	23^{+8}_{-6}
			$1.21^{+0.09}_{-0.09}$	>7.0	198^{+11}_{-13}	32^{+9}_{-7}
Field$_{\rm in}$	44	1.0	$0.84^{+0.22}_{-0.34}$	$2.5^{+1.1}_{-0.6}$	33^{+27}_{-15}	9^{+5}_{-4}
Field$_{\rm out}$	70	25.5	$1.20^{+0.14}_{-0.15}$	>9.6	166^{+17}_{-6}	15^{+7}_{-5}
GC$_{\rm ACS}$	36	0	$0.10^{+0.39}_{-0.62}$	$1.6^{+0.2}_{-0.2}$	11^{+2}_{-3}	$1.8^{+2.1}_{-1.2}$
GC$_{\rm D25}$	27	0	$0.41^{+0.39}_{-0.56}$	$1.6^{+0.2}_{-0.2}$	12^{+34}_{-3}	$2.5^{+2.8}_{-1.4}$

Note. Columns are as follows. (1) Population, (2) total number of sources observed above $L_{\rm lim} = 1.21 \times 10^{36}$ erg s^{-1}, (3) expected observed number of CXB sources above $L_{\rm lim}$ based on Georgakakis et al. (2008), (4) initial slope, (5) second slope, (6) break luminosity in units of 10^{36} erg s^{-1}, and (7) normalization (not normalized by the stellar mass). All errors and lower limits are at the 1σ level. Population descriptors: "total": all LMXBs within $(0.046-1.0)D_{25}$; "field": all LMXBs within $(0.046-1.0)D_{25}$, but excluding all 27 GC LMXBs and four GC LMXB candidates in the region; "field$_{\rm in}$": similar to "field" but only within $(0.046-0.2)D_{25}$; "field$_{\rm out}$": similar to "field" but only within $(0.2-1.0)D_{25}$; GC$_{\rm ACS}$: all *HST*/ACS GC LMXBs; and GC$_{\rm D25}$: all *HST*/ACS GC LMXBs within D_{25}. For the "total" and "field" XLFs, we give both the low-break and high-break solutions.
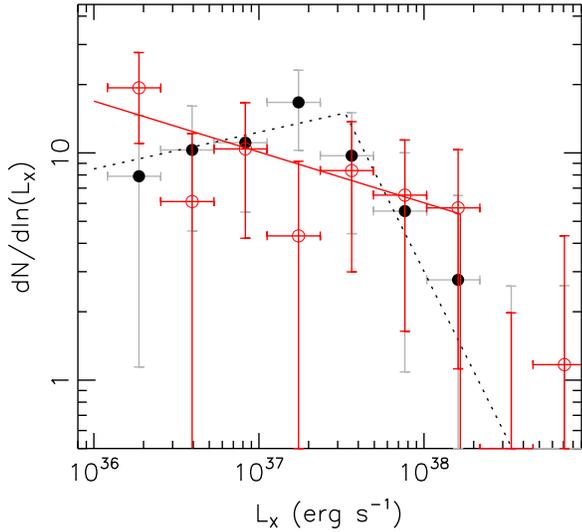

Figure 6. Incompleteness corrected and CXB contribution subtracted XLFs of field LMXBs within $\alpha/R_{25} = 0.046-0.2$ (filled circles) and those within $\alpha/R_{25} = 0.2-1.0$ (red open circles). Their best-fitting broken PL is shown as a dotted line and a red solid line, respectively.

the figure and given in Table 2. The XLF of field LMXBs in the inner region seems to be flatter at low luminosities, and the break seems to be at a lower luminosity than that in the outer region. We see no clear degeneracy in the fit; however the fit to the XLF from the inner region is similar to the low-break fit to the XLF from the whole region, and the fit to the XLF from the outer region is similar to the high-break fit to the XLF from the whole region, especially the break and second slope. The best-fitting α_1, $L_{\rm b}$, and α_2 of the XLFs in the inner and outer regions differ at the 1.5σ, 1.8σ, and 1.5σ confidence levels,
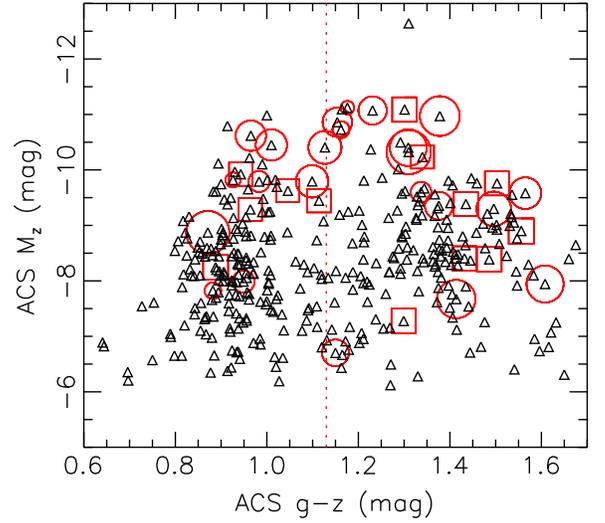

Figure 7. Color–magnitude diagram of *HST*/ACS GCs, with those containing LMXBs enclosed with squares ($L_{\rm X}$ within $(0.8-1.3) \times 10^{37}$ erg s^{-1}) or circles (others), whose size is proportional to the logarithm of the LMXB luminosity. The red dotted line at $g - z = 1.13$ mag was used by Jennings et al. (2014) as the dividing line between blue/metal-poor and the red/metal-rich subpopulations.

respectively. Such differences are marginally significant, and we discuss the possible origin in Section 4.

3.4. The XLF of LMXBs in GCs

The XLF for the LMXBs detected in *HST*/ACS GCs are shown in the right panels in Figure 5. It is incompleteness corrected using the incompleteness function (green dashed line) shown in Figure 4. The XLF of GC LMXBs seems flatter than that of field LMXBs. The fit with a broken PL is given in Table 2. We obtained $\alpha_1 = 0.10^{+0.39}_{-0.62}$, $\alpha_2 = 1.6 \pm 0.2$, and $L_{\rm b} = 11^{+2}_{-3}$, which are different from those from the field LMXBs (the low-break fit) by 2.5σ, 1.6σ, and 2.3σ, respectively. Our results agree with previous findings that the XLF of the field LMXB is steeper than that of GC LMXBs (Kim et al. 2009; Voss et al. 2009; Zhang et al. 2011), although the difference is not very significant in our case, owing to the relatively few GCs in our sample.

Previous studies of the XLF of GC LMXBs often just used sources within the D_{25} ellipse. We also obtained such an XLF for GC LMXBs, and the fitting results with a broken PL are given in Table 2. We obtained α_1, α_2, and $L_{\rm b}$ that were different from those from the field LMXBs (the low-break fit) by 1.5σ, 1.5σ, and 1.1σ, respectively. Due to fewer sources used, these differences are less significant than those reported using all *HST*/ACS GCs.

3.5. Optical Properties of GC LMXBs

Figure 7 plots the color–magnitude diagram of the *HST*/ACS GCs. To indicate the presence of LMXBs and their luminosity, we circle the 37 GCs containing LMXBs, with the size of the circle proportional to the logarithm of the LMXB luminosity. We enclosed the 13 GCs with $L_{\rm X}$ clusters within $(0.8-1.4) \times 10^{37}$ erg s^{-1} with squares instead. We note that all of our GC LMXBs have $L_{\rm X} > 1.13 \times 10^{36}$ erg s^{-1}. The median $(g - z)$ colors of GCs with LMXBs and without LMXBs are 1.23 and 1.06, respectively. Based on the nonparametric

Wilcoxon rank sum test, the difference is at a significance level of 2.7σ. Concentrating on luminous LMXBs with $L_X > 10^{37}$ erg s^{-1} (24 in total), we found that the median $(g - z)$ colors of GCs with luminous LMXBs and without luminous LMXBs are 1.31 and 1.05, respectively, corresponding to a Wilcoxon rank sum difference of 3.5σ. If we follow Jennings et al. (2014) and use $g - z = 1.13$ mag as the dividing line (dotted line in Figure 7) between the red/metal-rich and blue/metal-poor subpopulations, we find that 23 out of 169 (i.e., 13.6%) red GCs contain LMXBs, whereas there are 14 out of 191 (i.e., 7.3%) blue GCs containing LMXBs. Thus, the fraction of red GCs hosting LMXBs is about twice of that of blue GCs hosting LMXBs. Concentrating on luminous LMXBs with $L_X > 10^{37}$ erg s^{-1}, we find 18 (i.e., 10.7%) red GCs and six (i.e., 3.1%) blue GCs hosting luminous LMXBs. The former fraction is 3.5 times the latter, which is consistent with previous studies using a sample of galaxies with limiting X-ray luminosity around 10^{37} erg s^{-1} (Kundu et al. 2007; Sivakoff et al. 2007).

Figure 7 also shows that GCs hosting LMXBs tend to be bright/massive, as found previously for many galaxies (Kundu et al. 2007; Sivakoff et al. 2007; including NGC 3115, but using only the *Chandra* observation in 2001). The median M_z is -9.62 for GCs with LMXBs and -8.23 for GCs without LMXBs, corresponding to a Wilcoxon rank sum difference of 6.1σ. Similar results can be obtained if we just focus on luminous LMXBs with $L_X > 10^{37}$ erg s^{-1}, with the median M_z of -9.48 for GCs with luminous LMXBs and -8.29 for GCs without luminous LMXBs (the Wilcoxon rank sum difference is 4.4σ). Separating the GC subpopulations and concentrating on bright GCs with $M_z < -9.0$ mag, we find 16 out of 53 (i.e., 30%) red GCs and 10 out of 36 (i.e., 28%) blue GCs hosting LMXBs. For even brighter GCs with $M_z < -10$, we find 10 out of 14 (i.e., 71%) red GCs and three out of eight (i.e., 38%) blue GCs containing LMXBs. These fractions are significantly higher than those obtained for all GCs (i.e., 13.6% and 7.3% for red and blue GCs, respectively).

4. DISCUSSION

4.1. The Correction of CXB Contribution in XLFs

We obtained the XLFs of LMXBs in NGC 3115 down to $L_{lim} \approx 10^{36}$ erg s^{-1}, which has only been achieved for one other old galaxy (i.e., Centaurus A; Voss et al. 2009). We carried out careful corrections to the XLFs to account for the incompleteness effects and CXB contribution. We found no large discrepancy between the CXB density in our field and that estimated by Georgakakis et al. (2008), who used data from six large *Chandra* surveys. Even assuming a possible 20% enhancement of the CXB density in our field (Section 3.1), we found no noticeable effect on the XLFs. In some studies, the CXB contribution was taken into account by directly excluding CXB sources identified from the optical cross-correlation (e.g., Kim et al. 2009). We did not show the results using this method because our *HST* imaging is not deep enough. However, we also tested this method by excluding the active galactic nuclei (AGNs) that we identified in Paper II (about 50% of the expected number) and obtained XLFs very similar to the ones that we have shown. This is mainly because of the high inclination of NGC 3115, so that the CXB contribution is less significant for this galaxy than other typical ones.

4.2. Caveats on the XLF of Field LMXBs and Physical Implications

Our XLF of field LMXBs can be fitted with parameters typically seen in the literature for other old normal galaxies or the bulge of spiral galaxies, with a possible break around 5.7×10^{37} erg s^{-1}. Such a break has been attributed to different mechanisms of removal of orbital angular momentum (magnetized stellar wind versus gravitational wave emission; Postnov & Kuranov 2005) or different types of donor stars (giants versus main-sequence stars; Revnivtsev et al. 2011) in the high and low luminosities.

However, the interpretation of our XLF of field LMXBs is complicated by the presence of a degenerate solution with a high break at about 2×10^{38} erg s^{-1}. This degeneracy appears to be associated with a spatial variation of the XLF, with the XLF in the inner region $((0.046-0.2)D_{25})$ being flatter and having a lower break $(3 \times 10^{37}$ erg s$^{-1})$ than that in the outer region $((0.2-1.0)D_{25})$, which has a break around 1.7×10^{38} erg s^{-1}. Therefore, the XLF of field LMXBs in the inner region is closer to the XLF of GC LMXBs. One possible cause for this is that our field LMXB sample in the inner region could include some GC LMXBs that we cannot identify due to significant incompleteness effects near the galaxy center that limit our ability to detect GCs in the optical. In the outer region we found 25 LMXBs from 219 GCs and 44.5 in the field (after excluding the CXB contribution) above L_{lim}, but only two GC LMXBs from seven GCs and 43.0 field ones in the inner region. To have the same ratio of GC LMXBs to field LMXBs, we would have missed 22 GC LMXBs in the inner region. However, it is well known that the spatial distribution of GCs is more extended than the stellar light, as can also be seen in Figure 2 for the outer region. The distribution of GCs within $(0.3-1.3)D_{25}$, if fitted with a PL, is found to follow $\sqrt{\alpha/R_{25}}$, which would indicate that in the inner region there should be 93 GCs. Assuming the same detection rate of LMXBs (25/219 = 11.9%) as in the outer region, we would have missed 6.6 GC LMXBs, given that we detected two GC LMXBs and two candidates. Thus, the number of GC LMXBs that we missed in the inner region is probably small, compared with the total number of sources observed (43.0 after subtracting the CXB contribution), and their effect on the XLF of field LMXBs in the inner region should be insignificant.

Alternatively, the spatial variation of the XLF of field LMXBs might be real and can be explained if the field LMXBs in the inner region have a dynamical origin similar to GC LMXBs. There are two scenarios: one is the dynamical formation of LMXBs in the dense stellar environment near the galaxy nuclei, and the other is the destruction of GCs that drift toward the galaxy center due to mass segregation, leaving behind the remnant LMXBs. The former was argued to be the dominant mechanism to account for the high specific frequency of X-ray sources, per unit stellar mass (following the $\rho_{(*)}^2$ dependence on the stellar density), near the center ($<1'$) of M31 by Voss & Gilfanov (2007a, 2007b). However, we do not see increasing high specific frequency of (non-GC) X-ray sources at the very center, compared with the outer region (Figure 2). The stellar density of M31 is around $30 M_\odot$ pc^{-3} at $1'$ from the center (Voss & Gilfanov 2007b). Based on the stellar density model by Emsellem et al. (1999), we expect that NGC 3115 reaches a similar stellar density at $\alpha \sim 8''$ in the major-axis direction. Thus the former mechanism is probably still not significant in our inner region, which excludes the

central $a = 10''$ elliptical region. There is large uncertainty in estimating the level of the second mechanism. The specific frequency of (non-GC) X-ray sources seems to peak around $\alpha/R_{25} \sim 0.1$–0.2. If some part of it is due to the second mechanism, the remnant LMXBs should gain some momentum to reach this region during the destruction of GCs, or the destruction should be able to occur there.

Considering the possible contamination of the LMXBs from undetected or disrupted GCs in the inner region, the XLF in the outer region is probably a better representation of the characteristics of primordial field LMXBs. Its break at about 1.7×10^{38} erg s^{-1} (Table 2) seems somewhat higher (at the 90% confidence level) than the typical values of around 5×10^{37} erg s^{-1} reported in other studies that normally used most of the field (that is, no differentiation between the inner and outer regions; Gilfanov 2004; Kim et al. 2009; Voss et al. 2009; Zhang et al. 2012). Zhang et al. (2013) obtained XLFs combining 20 early-type galaxies for the inner and outer regions separately. Their inner and outer regions were defined as $(0.2$–$3)r_e$ and $(4$–$10)r_e$, respectively, where r_e is the K_s-band half-light radius. Our inner and outer regions for NGC 3115 are approximately $(0.3$–$1.3)r_e$ and $(1.3$–$6.5)r_e$, respectively. Visually it appears that the break of the XLF in their outer region is higher than the XLF in their inner region (see their Figure 4). However, they did not carry out the fit, and the significance of this variation is not clear. Moreover, they did not exclude GC LMXBs, making it difficult to compare directly. In the future, more galaxies should be used to investigate the XLF of field LMXBs from the outer region to check whether the high break that we observed in the XLF of field LMXBs in the outer region of NGC 3115 is universal or due to statistical fluctuation. If it is real, the best explanation is probably the Eddington limit of NS LMXBs. In Paper II, we showed that most of our bright LMXBs (above several 10^{36} erg s^{-1}) are NS LMXBs in the soft state.

In summary, the flatter XLF of field LMXBs in the inner region compared to that in the outer region is unlikely due to dynamically formed LMXBs in the dense stellar environment near the galaxy nucleus, but could be due to contamination of LMXBs from undetected and/or (more likely) disrupted GCs in the inner region. The field LMXBs in the outer region is more likely to be primordial. The break of their XLF could be due to the Eddington limit of NS LMXBs, which is in agreement with our finding in Paper II that most of our bright sources are NS LMXBs in the soft state.

4.3. Caveats on the XLF of GC LMXBs and Physical Implications

Considering the large detection rate of LMXBs ($\sim$71%, Section 3.5) in the most metal-rich and the most massive GCs, some of these GCs probably host multiple LMXBs that cannot be resolved by *Chandra*. We follow the method of Sivakoff et al. (2007) to study such source blending effects. They found the dependence of the expected number λ_t (assuming Poisson statistics) of LMXBs per GC on the GC properties to be:

$$\lambda_t = A \left(\frac{M}{10^6 M_\odot} \right)^{1.237} 10^{0.9(g-z)} \left(\frac{r_{h,M}}{1 \text{ pc}} \right)^{-2.22}, \quad (3)$$

where the GC mass is $M = 1.45 \times 10^{-0.4(M_z - M_{z,M_\odot})} M_\odot$ ($M_{z,M_\odot} = 4.512$) and the half-mass radius is $r_{h,M} =$
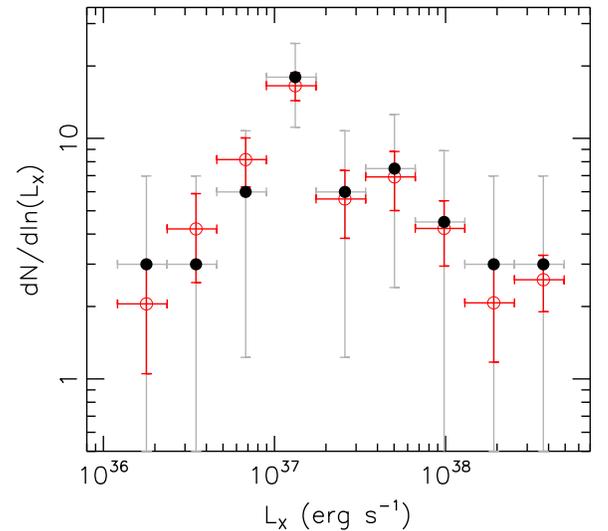

Figure 8. XLF of observed GC LMXBs (filled black circles) and the XLF using the mean of 1,000 simulations (open red circles, with the standard deviation as the error bar). The simulations take into account the possibility that some GCs might host multiple LMXBs (see the text). The XLFs were not corrected for the incompleteness effects.

$r_h \times 10^{0.17[(g-z)-1.22]}$. To match our observation of 37 GCs hosting LMXBs, the normalization, A, should be at least 0.16, without taking into account the incompleteness effects. The expected median M_z is then -9.36, which is slightly fainter than the observed value (i.e., -9.62, Section 3.5). Concentrating on the region of $M_z < -10.0$ and $(g-z) > 1.13$ where the LMXB detection rate is the highest, with 10 out of 14 GCs observed to host LMXBs (Section 3.5), the expected number of GCs hosting LMXBs from Equation (3) with $A = 0.16$ is 8.0, with the number of GCs expected to host multiple LMXBs $N_{multi} = 3.5$. The total expected number of LMXBs is $N_{LMXB} = 13.5$. To match the observed value of 10 GCs hosting LMXBs, A should be 0.25, resulting in $N_{multi} = 5.8$ and $N_{LMXB} = 21.6$ in this region. A similar exercise for the rest of the region (i.e., $M_z > -10.0$ or $(g-z) < 1.13$), shows that $A = 0.14$ could match the observed 27 GCs hosting LMXBs, with $N_{multi} = 3.4$ and $N_{LMXB} = 31.1$.

GCs hosting multiple LMXBs are expected to be more luminous and show less long-term variability in X-rays (Kundu et al. 2007). In the dense LMXB region of $M_z < -10.0$ and $(g-z) > 1.13$, there are four with the maximum 0.5–7 keV luminosity $>5 \times 10^{37}$ erg s^{-1}. They have 0.5–7 keV long-term luminosity variability of $V = 1.4, 1.4, 2.1,$ and 14.9. Among the field LMXBs within $(0.046$–$1.0)D_{25}$, there are 27 with a maximum 0.5–7 keV luminosity $>5 \times 10^{37}$ erg s^{-1}. Their median variability is 2.3, which is not significantly larger than that found for the GC LMXBs with high likelihood of blending. Thus we cannot confirm any effect of blending on the variability.

To investigate the source blending effects on the XLF, we carried out Monte Carlo simulations using Equation (3), with $A = 0.25$ if $M_z < -10.0$ and $(g-z) > 1.13$, and $A = 0.14$ elsewhere, as obtained previously. When a GC was simulated to host multiple LMXBs, we assumed them to have equal luminosities. The results from 1,000 simulations are shown in Figure 8, where we plot the XLF using the mean (open circles; the standard deviation is shown as the error bar) of LMXBs in

each luminosity bin from these simulations. The simulated XLFs seem steeper than the observed one overall, as expected. However, the difference is small, which is mainly due to two reasons: The first is that about a third of GC LMXBs are observed to cluster within a very narrow luminosity range $(0.8-1.4) \times 10^{37}$ erg s^{-1}, but these GCs are widely spread around in the color–magnitude diagram, thus producing no significant source blending effects. The second reason is that in the area of parameter space where GCs preferentially host LMXBs, both faint and luminous LMXBs were observed. That is, the source blending effects are seen at different luminosity levels. Therefore, we conclude that the source blending effects on the XLF are negligible, within the uncertainties of our data.

Instead of assuming equal weights to construct the XLF (Section 3.4), we explored the option of weighting the incompleteness function to reflect the tendency of LMXBs to be detected in metal-rich and massive GCs. We recalculated the XLF of GC LMXBs with the incompleteness function weighted by the probability of hosting one or more LMXBs, again based on Equation (3) with $A = 0.25$ if $M_z < -10.0$ and $(g - z) > 1.13$, and $A = 0.14$ elsewhere (although the source blending effects cannot be taken into account simultaneously). We find that the XLF obtained in this way shows no significant difference from that shown in Section 3.4.

Thus the observed paucity of faint GC LMXBs below the XLF break $\sim 10^{37}$ erg s^{-1} in NGC 3115 should be real. It could be explained if there is a transition from persistent sources to transients around this break (Kim et al. 2009; Voss et al. 2009). One main class of GC LMXBs could be ultracompact X-ray binaries (UCXBs). These are NSs accreting from white dwarf (WD) companions with very short orbital periods ($P_{orb} \lesssim 1$ hr) and might be effectively produced in GCs through direct stellar collisions between NSs and red giants (Verbunt 1987). Bildsten & Deloye (2004) first suggested that UCXBs with $P_{orb} \sim 8$–10 minutes could explain the XLF of GC LMXBs at high luminosities. The second slope ($\alpha_2 = 1.6 \pm 0.2$) that we obtained in the broken PL fit to the XLF is consistent with their prediction ($\alpha_2 = 1.77$). However, according to Lasota et al. (2008), for the transition from persistent to transient behavior for a He-rich X-ray irradiated accretion disk to occur at around 10^{37} erg s^{-1}, systems with $P_{orb} \gtrsim 40$ minutes are preferred, at least below the break luminosity.

It has been long-debated whether the entire population of LMXBs in galaxies, including those in the field, was formed dynamically in GCs (Kundu et al. 2002, 2007; White et al. 2002; Irwin 2005; Juett 2005; Humphrey & Buote 2008). Our result that the XLFs of GC and field LMXBs appear to be different agrees with previous findings (e.g., Kim et al. 2009; Voss et al. 2009; Zhang et al. 2011). The difference indicates that they are formed through different channels that result in different system configurations (orbital period, mass ratio, etc.) and thus with different mass accretion rates. Therefore, our result supports the idea that not all field LMXBs are formed dynamically in GCs.

In summary, source blending should occur in GC LMXBs, but we do not expect it to significantly affect the XLF. The observed paucity of faint GC LMXBs below the XLF break $\sim 10^{37}$ erg s^{-1}, compared with field LMXBs, is likely real, and one explanation is that GC LMXBs are dominated by accreting NSs with WD donors that show a transition from persistent sources at high luminosity to transients at low luminosity around this break. The different XLFs of GC and field LMXBs

suggest that field LMXBs are not all formed dynamically in GCs.

5. CONCLUSIONS

We studied the XLF of LMXBs in the early-type galaxy NGC 3115 using the the Megasecond *Chandra* XVP Observation of this galaxy. Including three previous observations, we obtained a total exposure of ~1.1 Ms and reached a detection sensitivity of $L_{lim} \sim 10^{36}$ erg s^{-1}, which is much lower than typically achieved for other early-type galaxies ($L_{lim} \sim 10^{37}$ erg s^{-1}) by *Chandra*. Our fit to the XLF of all LMXBs supports the presence of the low-luminosity break of the XLF at around 5.5×10^{37} erg s^{-1}, with the differential PL slope of 1.0 ± 0.1 and 2.2 ± 0.4 below and above the break, respectively, as seen in many previous studies (e.g., Gilfanov 2004; Kim et al. 2009; Voss et al. 2009; Zhang et al. 2012). However, we cannot exclude the possibility that the break is at around 1.6×10^{38} erg s^{-1} and is sharp, with the differential PL slope of 1.1 ± 0.1 and >6.7 below and above the break, respectively.

We further created the XLFs for field and GC LMXBs separately. Due to relatively few GC LMXBs, the XLF of the field LMXBs is very similar to the XLF of all (GC+field) LMXBs, and still shows degeneracy in the broken PL fit (one fit with a break at around 5.7×10^{37} erg s^{-1} and the other fit with a sharp break at around 2.0×10^{38} erg s^{-1}). The field LMXB XLF seems to show spatial variation, with the slopes and the break in the inner region ($(0.046-0.2)D_{25}$) being smaller than those in the outer region ($(0.2-1.0)D_{25}$). This could be due to the incompleteness effects of the optical GC detection in the inner region and/or contamination of remnant LMXBs left behind from the destruction of GCs that drift toward the galactic center due to mass segregation. The XLF from the outer region is thus probably closer to the XLF of primodial field LMXBs. It has a differential PL slope up to a break at around 1.7×10^{38} erg s^{-1}, which is close to the Eddington limit of NS LMXBs. The detection of spatial variation explains the degeneracy in our fit to the XLF from the whole study region.

The XLF of GC LMXBs overall is flatter than that of field LMXBs. Our observation of the difference between the XLFs of GC and field LMXBs casts doubt on the idea that all LMXBs in the galaxy are formed dynamically in GCs. The break of the GC LMXB XLF is at around 1.1×10^{37} erg s^{-1} and might be due to a transition from persistent sources at high luminosity to transients at low luminosity, which can be explained if GC LMXBs are dominated by accreting NSs with WD donors.

As in previous studies, we found that metal-rich/red GCs are more likely to host LMXBs than the metal-poor/blue ones, an effect that is more significant for more luminous LMXBs, and that more massive GCs are more likely to host LMXBs. Although source blending is likely to occur, our simulations indicate that it should not significantly affect the XLF.

During the end of the preparation of this paper, Lehmer et al. (2014) reported the study of three old normal galaxies. Their main goal was to test the evolutionary model of LMXBs, but they also obtained the XLFs of LMXBs in NGC 3115 using the same data presented here. In the appendix, we briefly compare our study with theirs. We found no large discrepancy between our results and theirs, if factors such as the fitting degeneracy and the possible spatial variation are taken into account.

APPENDIX
COMPARISON WITH LEHMER ET AL. (2014)

In their study of the evolutionary model of LMXBs, Lehmer et al. (2014) also presented the XLFs of LMXBs in three normal galaxies, including NGC 3115. They used the same data presented here for NGC 3115, but there are many differences between their analysis method and ours. Lehmer et al. used the limiting significance level of 10^{-5} for *wavdetect* and kept sources with false binomial probability less than 0.004 (see their Equation (1)), whereas we adopted the limiting significance level of 10^{-6} for *wavdetect* (Paper II) and used sources above $L_{\rm lim}$, which results in using only sources with the signal to noise ratio $\geqslant 2.9$. Moreover, Lehmer et al. used sources detected from the merged and individual observations (although the false binomial probability was calculated exclusively from the merged photometry), whereas we used sources detected from the merged observation only. Therefore we expect that Lehmer et al. could detect more real faint sources, but also more spurious faint sources than we did.

The region studied was also different. Lehmer et al. used an elliptical region of a semimajor axis of $2.'7$, a semiminor axis of $1.'1$, and a position angle of $45°$ (based on the *K*-band galaxy emission), excluding a central circular region of radius $20''$. We use the slightly larger D_{25} ellipse, excluding the central $a = 10''$ elliptical region. We excluded a smaller central region because of our use of subpixel binning images for source detection in the central region. Within their study region, we have 90 sources above $L_{\rm lim}$, among which 17.4 are expected to be CXB sources, whereas our study region has 145 sources above $L_{\rm lim}$, 26.5 of which are expected to be CXB sources. The handling of the CXB contribution in the fits to the XLFs is also different. Lehmer et al. excluded all AGNs that they could identify from the *HST*/ACS imaging (they found nine such sources, which is about 50% of the expected number), whereas we estimated the CXB contribution following Georgakakis et al. (2008).

We tried to check whether we could reproduce their XLF fitting results (they also fitted the XLFs with a broken PL) based on the sources that we detected, but using their study region. We followed their technique to exclude all AGNs that we could identify (10 from Paper II) from the *HST*/ACS imaging instead of estimating the CXB contribution following Georgakakis et al. (2008). We found that we generally obtained slightly lower values of the initial slope α_1 by (1–2) σ, most probably due to their inclusion of more very faint sources than were in our sample. Specifically, in the fit to the total XLF, they obtained $\alpha_1 = 1.5 \pm 0.1$, and we obtained $\alpha_1 = 1.3 \pm 0.1$ if we chose a high-break solution with $L_{\rm b} = 1.57^{+0.24}_{-0.53} \times 10^{38}$ erg s^{-1} similar to their $L_{\rm b} = (1.76 \pm 0.02) \times 10^{38}$ erg s^{-1}. We still see the degenerate low-break ($L_{\rm b} = (5.0 \pm 0.2) \times 10^{37}$ erg s^{-1}) fit, which has a C statistic larger than that of the high-break fit by only 0.4 (or by only 0.1 if the CXB contribution was subtracted from modeling

instead). For the field LMXB XLF, we preferred a high-break fit, which was also adopted by Lehmer et al. and is similar to our XLF of field LMXBs in the outer part of the D_{25} region (Section 3.3). For the GC LMXB XLF, they also obtained a high-break luminosity $L_{\rm b} = (1.76 \pm 0.19) \times 10^{38}$ erg s^{-1}, but we cannot constrain it well—$L_{\rm b} = 4.5^{+14.2}_{-3.6} \times 10^{37}$ erg s^{-1}; we have 22 GC LMXBs (including three candidates) above $L_{\rm lim}$ in their region, whereas they detected 25 GC LMXBs. Overall, we see no large discrepancy between our results and theirs for LMXBs in their study region. In addition, no large discrepancy is seen between our results for our study region and theirs, if factors such as the fitting degeneracy and the possible spatial variation are taken into account.

REFERENCES

Arnaud, K. A. 1996, in ASP Conf. Ser. 101, Astronomical Data Analysis Software and Systems V, ed. G. H. Jacoby & J. Barnes (San Francisco, CA: ASP), 17
Arnold, J. A., Romanowsky, A. J., Brodie, J. P., et al. 2011, ApJL, 736, L26
Bautz, M. W., Pivovaroff, M., Baganoff, F., et al. 1998, Proc. SPIE, 3444, 210
Bildsten, L., & Deloye, C. J. 2004, ApJL, 607, L119
Capaccioli, M., Held, E. V., & Nieto, J.-L. 1987, AJ, 94, 1519
de Vaucouleurs, G., de Vaucouleurs, A., Corwin, H. G., Jr., et al. 1991, Third Reference Catalogue of Bright Galaxies, ed. G. de Vaucouleurs et al. (New York: Springer)
Emsellem, E., Dejonghe, H., & Bacon, R. 1999, MNRAS, 303, 495
Fabbiano, G. 2006, ARA&A, 44, 323
Freeman, P. E., Kashyap, V., Rosner, R., & Lamb, D. Q. 2002, ApJS, 138, 185
Georgakakis, A., Nandra, K., Laird, E. S., Aird, J., & Trichas, M. 2008, MNRAS, 388, 1205
Gilfanov, M. 2004, MNRAS, 349, 146
Grimm, H.-J., Gilfanov, M., & Sunyaev, R. 2003, MNRAS, 339, 793
Humphrey, P. J., & Buote, D. A. 2008, ApJ, 689, 983
Irwin, J. A. 2005, ApJ, 631, 511
Jarrett, T. H., Chester, T., Cutri, R., Schneider, S. E., & Huchra, J. P. 2003, AJ, 125, 525
Jennings, Z. G., Strader, J., Romanowsky, A. J., et al. 2014, AJ, 148, 32
Juett, A. M. 2005, ApJL, 621, L25
Kalberla, P. M. W., Burton, W. B., Hartmann, D., et al. 2005, A&A, 440, 775
Kim, D.-W., & Fabbiano, G. 2003, ApJ, 586, 826
Kim, D.-W., & Fabbiano, G. 2004, ApJ, 611, 846
Kim, D.-W., Fabbiano, G., Brassington, N. J., et al. 2009, ApJ, 703, 829
Kundu, A., Maccarone, T. J., & Zepf, S. E. 2002, ApJL, 574, L5
Kundu, A., Maccarone, T. J., & Zepf, S. E. 2007, ApJ, 662, 525
Lasota, J.-P., Dubus, G., & Kruk, K. 2008, A&A, 486, 523
Lehmer, B. D., Berkeley, M., Zezas, A., et al. 2014, ApJ, 789, 52
Li, J., Kastner, J. H., Prigozhin, G. Y., et al. 2004, ApJ, 610, 1204
Lin, D., Irwin, J. A., Wong, K.-W., et al. 2015, ApJ, 808, 19
Luo, B., Fabbiano, G., Fragos, T., et al. 2012, ApJ, 749, 130
Mineo, S., Gilfanov, M., & Sunyaev, R. 2012, MNRAS, 419, 2095
Monet, D. G., Levine, S. E., Canzian, B., et al. 2003, AJ, 125, 984
Postnov, K. A., & Kuranov, A. G. 2005, AstL, 31, 7
Revnivtsev, M., Postnov, K., Kuranov, A., & Ritter, H. 2011, A&A, 526, A94
Sánchez-Blázquez, P., Gorgas, J., Cardiel, N., & González, J. J. 2006, A&A, 457, 809
Sarazin, C. L., Irwin, J. A., & Bregman, J. N. 2001, ApJ, 556, 533
Sivakoff, G. R., Jordán, A., Sarazin, C. L., et al. 2007, ApJ, 660, 1246
Tonry, J. L., Dressler, A., Blakeslee, J. P., et al. 2001, ApJ, 546, 681
Verbunt, F. 1987, ApJL, 312, L23
Voss, R., & Gilfanov, M. 2007a, A&A, 468, 49
Voss, R., & Gilfanov, M. 2007b, MNRAS, 380, 1685
Voss, R., Gilfanov, M., Sivakoff, G. R., et al. 2009, ApJ, 701, 471
Weisskopf, M. C., Brinkman, B., Canizares, C., et al. 2002, PASP, 114, 1
White, R. E., III, Sarazin, C. L., & Kulkarni, S. R. 2002, ApJL, 571, L23
Wong, K.-W., Irwin, J. A., Shcherbakov, R. V., et al. 2014, ApJ, 780, 9
Zhang, Z., Gilfanov, M., & Bogdán, Á 2012, A&A, 546, A36
Zhang, Z., Gilfanov, M., & Bogdán, Á 2013, A&A, 556, A9
Zhang, Z., Gilfanov, M., Voss, R., et al. 2011, A&A, 533, A33